Dissociative Ionization of Na_2 via Repulsive Rydberg States: Elucidating Femtosecond Dynamics with Nanosecond Lasers†

Hong Chen and Lutz Hüwel*

Physics Department, Wesleyan University, Middletown, Connecticut 06459

Received: March 18, 2008; Revised Manuscript Received: May 20, 2008

We have studied the dissociative ionization behavior of Na_2 molecules using two-color, three photon optical-optical double resonance enhanced excitation via the $A^1\Sigma_u^+$ and the $2^1\Pi_g$ states. Excess energy ranges from about 150 to about 1500 cm^{-1} above threshold for dissociative ionization into ground-state Na and Na^+. Slow atomic Na^+ fragments and Na_2^+ molecular ions are detected using a linear time-of-flight spectrometer operated in low field extraction, core sampling mode. To explain the observed energy dependence of the Na^+/Na_2^+ branching ratio, we introduce a semiclassical model for the underlying decay dynamics. Franck−Condon overlap densities for bound−free transitions starting in $2^1\Pi_g$ vibrational levels indicate that atomic Na^+ fragments are primarily produced via Rydberg states, with principal quantum number n between 5 and 12, converging to the repulsive $1^2\Sigma_u^+$ first excited-state potential of Na_2^+. Dynamics along these Rydberg curves involves competition between electronic (autoionizing) and nuclear (dissociative) degrees of freedom. Within the model, the autoionization lifetime τ_{auto} is the only one free parameter available to fit calculated Na^+/Na_2^+ branching ratios as a function of excess energy to the observed values. The lifetime is assumed to be the same multiple c of the Bohr period of each Rydberg potential. A χ^2-minimization procedure yields, for the range of principal quantum numbers involved, a most likely value of $c = 1.5 \pm 0.3$, implying that on average the Rydberg electron completes only 1 to 2 orbits before interaction with the excited core electron leads to autoionization.

Introduction

In the work described here, we have investigated the competition between nuclear and electronic degrees of freedom in the context of sodium dimer dissociative ionization near its lowest threshold at 47471.480 cm^{-1} above the ground state. We find that dissociative Rydberg states, converging to the $1^2\Sigma_u^+$ potential of the sodium cation Na_2^+ play a significant role in the production of atomic Na^+ ions. The competition between electronic autoionization and nuclear dissociation occurs on subpicosecond timescales. In this paper we demonstrate that a classical model that mimics the dynamics of wavepackets excited on these Rydberg states can successfully reproduce observed Na^+:Na_2^+ ratios. In particular, we extract autoionization lifetimes that are about 1.5 times larger than the corresponding Bohr orbit periods. For the principal quantum numbers of the Rydberg states involved, about 5−10, we thus find absolute autoionization lifetimes from about 30 fs to about 230 fs.

Superexcited states of molecules such as these Rydberg states are short-lived electronic resonances that play important roles in various molecular processes such as dissociative electron−ion recombination,[1–3] associative ionization,[4,5] and dissociative photoionization.[6,7] These resonances may be regarded as the electronic analog to transition states in molecular dynamics connecting reactants and products to each other.[8,9] For example, collisions of two sufficiently excited atoms can carry them along suitable potential curves such that at sufficiently close internuclear distances their combined electronic energy is above that of the lowest molecular ion state. In that case, intramolecular electron−electron interactions can lead to associative ionization and the ejection of one of the electrons. The time reversed process, dissociative recombination, involves the temporary capture of an incoming electron in one of these superexcited or dissociative Rydberg states that must be stable enough or the repulsive force on the atomic constituents of the molecule must be strong enough so that nuclear dissociative motion can separate the atoms fast enough to a critical distance beyond which autoionization is energetically no longer possible. This process is not only relevant for the light hydrogen molecule but is also of general importance in dissociative recombination, which has been reaffirmed in several recent review papers. These short-lived electronic resonances are also accessible by photoexcitation of neutral precursor states leading to the formation of molecular and atomic ions or neutral atomic fragments that include electronically excited states. This approach, also taken in the current paper, has the advantage that at least in principle the superexcited-state region can be explored systematically and with good energy resolution. Often UV or X-ray excitation is employed to very high lying parts of dissociative curves where repulsive forces are strong and thus nuclear motion of even heavy atoms can compete with swift electronic motion. Alternatively, one can slow down the electronic motion by excitation into superexcited states involving high Rydberg states. Alkali molecules in particular with their highly accessible states offer fertile ground for such an approach. In the current experiment, we explore, with the help of two color, three photon double resonance excitation via the $A^1\Sigma_u^+$ and $2^1\Pi_g$ states of Na_2, the energy range from near threshold to approximately 1500 cm^{-1} above threshold for Na_2 dissociative ionization into ground state Na^+ and Na. Quantum chemists have taken impressive strides in the capacity to calculate molecular electronic potential curves beyond the ground state. In particular for the hydrogen and alkali

† Part of the "Stephen R. Leone Festschrift".

* Corresponding author. E-mail: lhuwel@wesleyan.edu.

10.1021/jp802342d CCC: $40.75
Published on Web 07/09/2008

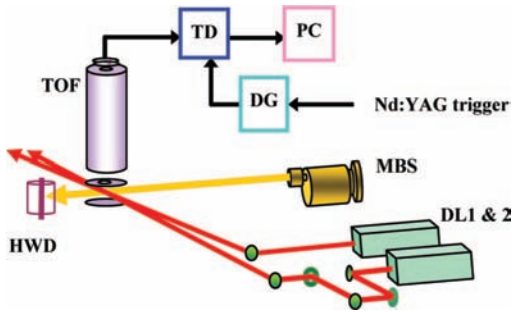

Figure 1. Schematic experimental setup with main components: MBS, molecular beam source; HWD, hot wire detector to monitor beam intensity; DL 1 and 2, pump (1) and probe (2) pulsed dye lasers; TOF, time-of-flight mass spectrometer; DG, digital delay generator; TD, 100 MHz transient digitizer; PC, desktop computer.

dimers a large array of excited-state calculations exists including states with unusual shapes due to interactions and avoided crossings with other potentials.[10,11] However, electronic states that involve autoionization bring another range of complexity and much fewer calculations for such states exist. Some examples include the calculation of resonance parameters and quantum defects for superexcited states in molecular hydrogen,[12] doubly excited potential curves responsible for associative ionization in Na(3p) + Na(3p) collisions,[13] and at least a qualitative discussion[14] of molecular potentials derived from the Na(3p) + Na(4s) pair that lie entirely in the autoionizing continuum of the Na_2^+ ground state potential. The last example is particularly interesting in our context because these potentials were used to explain previous femtosecond experiments[15,16] that had observed atomic Na^+ ion formation at around 600 to 1200 cm^{-1} above threshold after excitation out of the $2^1\Pi_g$ state. This is the same intermediate state and about the same above threshold energy range explored in our nanosecond experiments described here. We do not see obvious evidence of such doubly excited states in our data, such as a change in total ion yield or atomic to molecular ion yield ratio, when we tune the energy through its expected potential minima. Nevertheless, we cannot rule out that it plays a rule in some subtle ways. The role of repulsive Rydberg states has been indicated previously to play a potential role in dissociative ionization processes for both sodium[17,18] and hydrogen dimers.[19]

Experimental Approach

The experiments described here have been performed in our molecular beam setup described previously[20,21] and schematically depicted in Figure 1. A mild supersonic expansion of neat sodium from a double chamber molecular beam source (MBS in Figure 1) is collimated into a narrow beam with residual full angular divergence of about 7 mrad. Source conditions as well as careful measurements of the deflection of Na_2^+ ions by horizontal electric fields indicate a speed ratio of $S = 2$ and beam temperature of $T = 50-100$ K, corresponding to a most probable speed of the Na_2 dimer of about 600 m/s. Under these conditions, dimer molecules are expected to constitute about 5−10% of the beam particles with small amounts of trimers and negligible traces of larger clusters.[22]

After the last collimation aperture, the molecular beam enters a differentially pumped chamber with a base pressure of 1×10^{-7} Torr. Here, the beam particles are illuminated by two laser beams, crossing perpendicular to the molecular beam direction. Both lasers are tunable dye lasers with a grazing incidence Littman configuration. They are pumped by the split 532 nm output of a single 20 Hz Nd:YAG laser. The first dye laser (laser 1) is home-built and operates with a mixture of Rhodamine R610 and R640 dyes. The bandwidth of this laser is only about 0.6 cm^{-1}. Laser 1 pumps Na_2 molecules from the vibrational ground state $v'' = 0$ of the $X^1\Sigma_g^+$ electronic ground state to well-defined ro-vibrational levels of the first excited $A^1\Sigma_u^+$ state. For the results reported in this paper, we excite vibrational levels $v' = 16-18$ and rotational levels $J' = 24$ and 30, requiring a wavelength range for laser 1 from roughly 605 to 610 nm. The second dye laser (laser 2) is a commercial instrument with a bandwidth of about 0.1 cm^{-1}. Using DCM dye, laser 2 excites the Na_2 molecules from the $A^1\Sigma_u^+$ to the $2^1\Pi_g$ state with final vibrational levels between $v = 14$ and 22, corresponding to a wavelength range from approximately 620 to 655 nm for laser 2. Both dye lasers are linearly polarized in the vertical direction except for the polarization dependence measurement discussed below. Ionization out of the pumped vibrational levels of the $2^1\Pi_g$ state can be achieved with one additional photon from either dye laser. Therefore, to establish a well characterized situation, we send laser 2 on a 3 m detour relative to laser 1, thereby introducing an optical delay of about 10 ns, equivalent to about one pulse duration, between pump (laser 1) and probe (laser 2). Laser powers are adjusted so that in almost all cases none of the two lasers alone generates ions. Nevertheless, in a few instances the pump laser alone does create a small ion signal (the probe laser never does). Thus, we record spectra both with pump only and with pump and probe present and subtract the former from the latter.

Ions produced by the lasers are mass selected by a Wiley−McLaren type linear time-of-flight (TOF) mass spectrometer[23] and detected by microchannel plates in a Chevron configuration. In the experiments discussed here, the extraction and acceleration field strengths are about 30 and 75 V/cm, respectively, for the yield measurements and a factor of 4 lower for the polarization dependence data. Yield measurements are obtained by feeding the signal into two gated boxcar integrators, and time-resolved spectra are recorded with the help of a PC controlled 100 MHz transient digitizer. The two boxcar gates are appropriately delayed to coincide with the atomic or molecular ion signal, respectively. Both gate widths are set to 300 ns a length, which covers the complete flight time ranges in question: about 30 ns for Na_2^+ and about 200 ns for the Na^+ fragments.

Findings. Figure 2 represents an example of the mass selected ion yield spectra we have recorded when the probe laser is tuned through the rotational resonances of a specific $A^1\Sigma_u^+$ to $2^1\Pi_g$ vibrational transition. In the case shown in this figure, the ions are produced with the probe laser exciting the $v = 19$ vibrational level of the $2^1\Pi_g$ state of Na_2, which in turn is excited with the pump laser tuned (and held fixed) to the $v' = 16$ vibrational level of the $A^1\Sigma_u^+$ state. Rotational and vibrational quantum numbers are uniquely assigned by comparing measured wavenumber intervals between the P, Q, and R components with theoretical values derived from published spectroscopic data.[24] A corresponding approach is used to make the assignment for the pump laser excitation, using the most recent spectroscopic data sets available for both the $X^1\Sigma_g^+$ electronic ground state[25] and the $A^1\Sigma_u^+$ state.[26] Because of the relatively broad bandwidth of the pump laser, excitation out of the $v'' = 0$ vibrational level of the ground $X^1\Sigma_g^+$ state is not completely rotationally resolved. In each of the transitions we investigated, we pump into two different rotational levels in the $A^1\Sigma_u^+$ state. For $v' = 16$ and 17, these rotational states are $J' = 24$ and 30 and for $v' = 18$ they are $J' = 20$ and 26. Therefore, the probe laser excitation

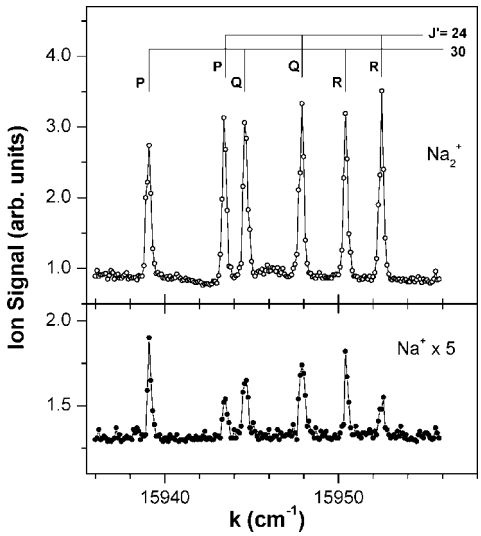

Figure 2. Sample mass selected ion yield spectrum showing Na_2^+ (upper panel) and Na^+ (lower panel) ion yields as a function of probe laser wavenumber; the case shown was obtained by exciting from vibrational level $v' = 16$ in the $A^1\Sigma_u^+$ state to vibrational level $v = 19$ in the $2^1\Pi_g$ state.

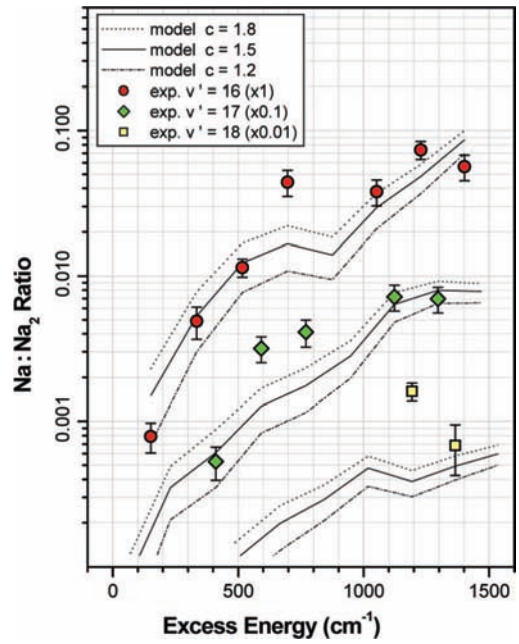

Figure 3. Variation of Na^+:Na_2^+ ion yield ratio with excess energy above dissociative ionization threshold. Experimental results (symbols) for excitation out of vibrational levels $v' = 16$, 17 and 18 in the $A^1\Sigma_u^+$ state are compared with corresponding model calculations (lines) for three different scaling factors of the autoionization lifetime.

from the $A^1\Sigma_u^+$ to the $2^1\Pi_g$ state reveals six final rotational levels, corresponding to the *P*, *Q* and *R* branches for each of the two rotational levels in the $A^1\Sigma_u^+$ state (see Figure 2). After careful exploratory experiments to establish viable excitation and detection conditions, we settled on the excitation sequences $v' = 16$ to $v = 14-21$, $v' = 17$ to $v = 14-21$, and in a separate run the two transitions $v' = 18$ to $v = 21$ and 22. Each of these transitions has a unique and well characterized excess energy value (see below for details). Due to weak Franck−Condon factors, crowded excitation spectra, and/or experimental difficulties, we did not obtain useful yield spectra for the $v' = 16$ to $v = 18$ and the $v' = 17$ to $v = 19$ transitions and we did not detect observable atomic ion signal in the $v' = 17$ to $v = 14$ and 15 transitions. In all other cases, the ion signal strength was sufficient for subsequent analysis to be included in the Na^+:Na_2^+ ratio plots shown in Figure 3. As can be seen from this figure, the maximum value of the measured ratio of atomic to molecular ions is only 0.07−0.08 for the $v' = 16$ and 17 sequences and reaches 0.16 for the $v' = 18$ to $v = 21$ case. In general, the ratios decrease with decreasing excess energy becoming as low as 0.001 to 0.005 near threshold. Within our measured data set, the high ratio value for the $v' = 18$ to $v = 21$ transition seems to be an anomaly and is not explained by the model.

All Na^+:Na_2^+ ratio values shown in Figure 3 are obtained directly from ion yield spectra such as the one shown in Figure 2. From the always strong molecular ion signal we find appropriate wavenumber intervals to sum the intensity of each of the six rotational lines. These same limits are then used to extract atomic ion intensities from the corresponding Na^+ yield spectra. Application of baseline subtraction and overall detection efficiency correction (consisting of boxcar sensitivity setting and TOF collection efficiency) then yields six separate ratios for each transition. Because we cannot discern a rotational dependence pattern in our data, we average all six results to obtain the final ratio value for each of the excess energy values shown in Figure 3. We have repeated each measurement at least once and, for a few test cases, we performed more extensive reproducibility checks. Typically, the variability of the final outcome is about 10−15%. Because the measured atomic ion peaks in particular contain only about five data points, we also used a Gaussian linefit routine to extract the ion yield values. Both approaches, direct summing and linefit, give the same result well within the estimated uncertainty discussed below.

The second factor entering the overall detection efficiency correction, the TOF collection efficiency, deserves a more detailed discussion because it influences the final ratio values noticeably. For the extraction and acceleration voltages used in our experiment, the value of this collection efficiency is different for atomic and molecular ions and changes with kinetic energy and angular distribution of the atomic ion fragments. We have explored these dependencies with the help of a Monte Carlo simulation program that we have developed for our experiment and that has been tested in several previous experiments in both our laboratory[20] and in a collaboration project.[27] From our previous dissociative ionization experiments, we have learned in particular that because of our relatively low extraction fields the angular distribution of the fragments matters. Therefore, we performed auxiliary experiments to determine the angular distribution patterns for the current situation. To this end, we record TOF spectra for different orientations of the linear polarization direction of both pump and probe laser. Extraction and acceleration voltages are lowered by a factor of 4 relative to the yield experiments, which "stretches" features in the flight time spectra, thus enhancing any changes with polarization. One example of such a TOF spectrum, for the same $v' = 16$ to $v = 19$ transition as in Figure 2, is shown in Figure 4. First, the width of the Na^+ peak is consistent with the expected energy release in this transition. Note that because of the lower TOF field strengths used in Figure 4, this width now exceeds the 300 ns boxcar gate used in the yield experiments. Figure 4 illustrates also the absence of any significant ion production by the probe laser only. This is typical for the pump laser as well and for most other transitions investigated (see above). Finally, as already implied, Figure 4 reveals that there is a significant change when the laser polarization is rotated and that there is indeed an anisotropic fragment distribution. Specifically, the increased flux at early and late flight times of the Na^+ ion peak

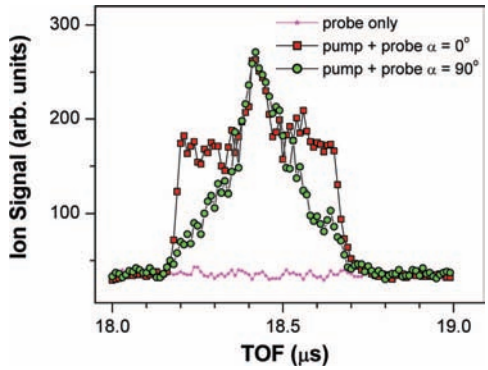

Figure 4. Experimental time-of-flight (TOF) spectrum showing atomic ion signal for vertical ($\alpha = 0°$) and horizontal ($\alpha = 90°$) laser polarizations. Also shown is a background spectrum taken with only the probe laser present.

for all vertical polarization ($\alpha = 0°$ case in Figure 4) relative to the all horizontal case ($\alpha = 90°$) indicates enhanced fragment flux along the laser polarization. A detailed analysis of the angular distribution experiments is beyond the scope of this paper. In the current context of the collection efficiency, it suffices to say that we can characterize the angular distribution by a case close but not entirely equal to a $(\cos\theta)^2$ dependence with θ the polar angle between fragment velocity and laser polarization in the body-fixed reference frame. This corresponds to the usual anisotropy parameter[28] β having a value between 0 and 2. Given these constraints, we can model the observed TOF spectra and derive collection efficiencies that vary monotonically with fragment excess energy from essentially 1 near threshold to about 0.75 at 1500 cm^{-1}, the upper energies explored here. Because the angular distribution is currently not yet fully characterized, we use the average of the collection efficiencies calculated for $\beta = 2$ and 0, a range which definitely includes the observed angular distribution pattern. Varying the thus obtained collection efficiencies by ±20% covers both β cases. The vertical bars included in Figure 3 reflect the corresponding range of Na^+:Na_2^+ ratios. Although the estimated overall uncertainty in these ratios is thus quite substantial (probably of the order of 30%), the overall trend with excess energy is still clear and the order of magnitude remains quite sensitive to the autoionization rate as will be discussed in the section detailing our classical model calculations also displayed in Figure 3.

However, before we can proceed we need to explain how the excess energy for each of the experimental results in Figure 3 is obtained. Because of the optical delay between pump and probe laser, any observed ions are produced by one photon from the pump and two photons from the probe laser. Although the probe laser power density must be high enough to allow absorption of two photons, we can rule out ion formation from higher order processes. Fragment energies as measured by TOF spectra, such as the one shown in Figure 4, as well as the absence of detectable ion signal with only the probe laser present both speak clearly against such ion production. Thus, because of the unambiguous assignment of all intermediate levels and the availability of precise spectroscopic parameters, we can calculate the excess energies ΔE straight forwardly and very accurately with the following formula

$$\Delta E = (E(v''=0,J'') + hf_1 + 2hf_2) - (D_0(X^1\Sigma_g^+) - \mathrm{IP(Na)}) \quad (1.1)$$

where $E(v'=0,J'') = E_{rot}(J'')$ is the rotational energy of the vibrational and electronic ground state from which the pump

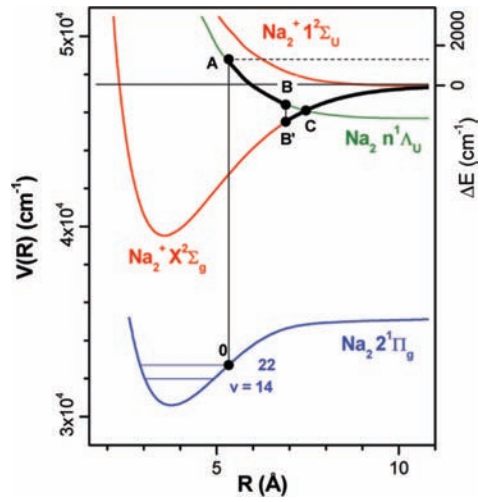

Figure 5. Schematic representation of indirect dissociative ionization, including third photon absorption at 0 and subsequent classical molecular dynamics starting at A. Dissociation along repulsive Rydberg state is interrupted at B by autoionization to B′ and is completed by motion along the Na_2^+ ground-state potential (see text for details).

laser excites with photon energy hf_1 into ro-vibrational level v',J' of the $A^1\Sigma_u^+$ state, hf_2 is the corresponding photon energy of the probe laser tuned to the transition from this level to level v,J of the $2^1\Pi_g$ state, $D_0(X^1\Sigma_g^+)$ is the dissociation energy of the Na_2 ground state, and IP(Na) is the ionization energy of atomic Na. Using the most recent spectroscopic data for the $X^1\Sigma_g^+$ state,[25] the $A^1\Sigma_u^+$ state,[26] the $2^1\Pi_g$ state,[24] groundstate molecular dissociation energy[29] and atomic ionization potential,[30] uncertainty in the excess energy values stems from the fact that our experimental results for each transition are averages of the *P*, *Q* and *R* branches of the two different rotational levels of the $2^1\Pi_g$ intermediate state. For the specific numbers involved, this range is found to be somewhat less than ±30 cm^{-1}; which is about the width of the symbols in Figure 3.

Semiclassical Model. To gain more insight into the physics underlying our observations, we developed a semiclassical model that takes its cue from an early theory of dissociative attachment.[31] The essence of this model can most easily be understood with the help of Figure 5. In essence, we assume excitation of the OODR prepared ro-vibrational level of the $2^1\Pi_g$ state into the manifold of repulsive Rydberg states converging toward the $1^2\Sigma_u^+$ potential of the Na_2^+ molecular ion. This is depicted as the transition from point 0 to point A in Figure 5 for one arbitrary choice of these Rydberg states. Immediately afterward, classical motion along the potential curve ensues. This takes the molecule from point A toward the asymptotic limit of two neutral Na atoms with one in the 3s ground state and one in an excited-state characterized by principal quantum number *n* and angular quantum number *l*. Any fine and hyperfine structure is ignored. As long as the dissociative trajectory has not yet crossed point C, where the Rydberg state becomes energetically lower than the ion ground state, electronic autoionization onto the $X^2\Sigma_g^+$ electronic ground state of the ion is possible. If that happens, e.g., at point B, the Rydberg electron interacts with the excited core electron and exchange energy is used to free the Rydberg electron and to de-excite the core electron to its ground-state orbital. Thus the molecule jumps from point B to point B′ and continues its motion, with the same kinetic energy it had at point B, along the $X^2\Sigma_g^+$ ground-state potential. The ultimate fate of the ion depends on the ratio of this kinetic energy to the binding energy of the molecular ion in point B′. If this ratio is less than 1, the ion remains bound

and autoionization leads to vibrationally excited Na_2^+ molecular ions. If this ratio is larger than 1, the ion will dissociate and autoionization leads to Na^+ atomic ion formation. Clearly, if the autoionization transition BB′ occurs near the starting point A, kinetic energy will be low and only molecular ions can be produced. On the other hand, at point C the kinetic energy is obviously sufficient to climb up the asymptotic limb of the $X^2\Sigma_g^+$ potential and to produce atomic fragments with excess energy ΔE numerically equal to the energy of point A above the threshold for dissociative ionization (incidentally, at point C, the exchange energy is exactly equal to the Rydberg electron binding energy). Therefore, there exists a critical point between A and C such that any autoionization event occurring between A and this point leads to molecular ions and to atomic ions if it occurs between the critical point and point C. Evidently, the magnitude of the autoionization lifetime, τ_{auto}, relative to that of the dissociation time from point A to C, τ_{AC}, determines both absolute ion yield and the ratio of atomic to molecular ions. If τ_{auto} is much smaller than τ_{AC}, i.e., if autoionization is very rapid, almost no neutral fragments will be produced and almost all ions will be molecular. If τ_{auto} is much larger than τ_{AC}, very few ions will be formed. However, now the share of atomic fragments will be larger. For values of τ_{auto} in between, the absolute atomic ion yield (as opposed to the Na^+:Na_2^+ ratio) will have a maximum.

Before a more detailed discussion of the implementation of the model is offered, we want to address its limitations and the question why a classical approach is applicable in the first place. Usually, nanosecond lasers can excite the Na_2 molecule only into single ro-vibrational levels or into scattering wave functions over a narrow energy range in a single continuum, ignoring again any electronic and nuclear spin effects. However, in the case of repulsive Rydberg states, every horizontal line above the dissociative ionization threshold ($\Delta E = 0$ on the right vertical axis in Figure 5) slices through *all* states converging to the $1^2\Sigma_u^+$ potential. Thus, depending on Franck−Condon factors and transition dipole moments, each photon absorbed by a Na_2 molecule in the $2^1\Pi_g$ state leads to the coherent excitation of several different electronic states. These states differ in both the electronic and the nuclear part of their wave functions: in general, they will have different principal and electronic angular momentum quantum numbers, and the atomic fragments will generally have different asymptotic translational and rotational kinetic energies. Thus, in a first approximation, one can think of the absorption step 0−A in Figure 5 as leading to the generation of an electronic and nuclear wavepacket pair whose dynamics is coupled but whose overall energy is (reasonably) well-defined. In addition, autoionization adds a nonadiabatic feature and, if it occurs, causes motion to switch to the molecular ion ground state. A quantum mechanical picture would need to incorporate all of these aspects as well. This is definitely outside our expertise; instead, we adopted the classical model introduced above, developing it as fully as we could. But even with this modest goal, simplifications are unavoidable. For example, there is no information available about the exact shape of the Rydberg states in question. Likewise, autoionization rates in this region are not known. Furthermore, as mentioned in the Introduction, the Na_2 molecule has a rich electronic structure near the dissociative ionization threshold and doubly excited states as well as excited negative ion positive ion pair potentials might play a role. For example, assumption of a simple Coulomb interaction between the Na^+ ground state and the 3p3d ^3F and 3p4s ^3P + 3p3p ^3D Na^- resonances leads to a crossing of the $\Delta E = 0$ threshold by this potential at around $R = 5.6$ and 6.8 Å, respectively, close to the crossings of the 7f and 12f Rydberg curves (we compare here with manifold Rydberg states, but Rydberg potentials with lower angular momentum are also nearby). Furthermore, doubly excited states connected to the Na(3p)−Na(4s) pair have been invoked as contributors to dissociative ionization observed in femtosecond experiments[15,16] involving vibrational wavepackets in the $2^1\Pi_g$ state. A figure of preliminary calculations[14] of these states (no definitive results were ever published) indicates that a $^1\Pi_u$ curve has its potential minimum at $R_{min} \approx 4.7$ Å and approximately 500 cm^{-1} above threshold; this would be at a location crossed, for example, by the 5f Rydberg potential. At higher excitation energies, associative ionization between Na(3p) and Na(3d) atoms has been reported,[32] indicating that such doubly excited states are indeed a factor for near threshold molecular dynamics. Nevertheless, at this time our model disregards all such potentials and their possible influences on our experiment. Thus, it is a distinct possibility that some of the features in our results are influenced by these omitted potentials. Finally, we have ignored the most obvious channel for Na^+ formation, direct one-photon access from the pumped vibrational levels of the $2^1\Pi_g$ state to the continuum of the $X^2\Sigma_g^+$ potential of the Na_2^+ molecular ion. The reason for this exclusion lies in unfavorable Franck−Condon densities. Crudely speaking, from threshold to about 1500 cm^{-1} above, de Broglie wavelengths of the $X^2\Sigma_g^+$ continuum states are smaller by a factor of about 2 than the ones of the $2^1\Pi_g$ vibrational wave functions of interest. Thus, one can expect that destructive interference will lead to small values of the overlap integrals. This is indeed borne out in numerical evaluations. We find Franck−Condon densities for $X^2\Sigma_g^+$ continuum states that are at least 3 orders of magnitude lower than the corresponding values for Rydberg states having the largest overlaps with the initial $2^1\Pi_g$ vibrational level. Although the transition dipole moment could increase this ratio, we felt justified to ignore the influence of direct ionization in our model.

We will now turn to the details of how the classical model described above is implemented in the current situation. The prerequisite potential curves for our classical dynamics calculation are obtained by fitting a flexible functional form to theoretical results for the two Na_2^+ potentials. Published results for these potentials[33−36] do not differ significantly, and we chose those by Masnou−Seeuws and Magnier as they provide a fairly dense list of data points. Our experiments are only sensitive to the portions of the potential at larger internuclear distance and in particular to the repulsive parts. Apart from some photodissociation[37] and dissociative ionization experiments,[20] these potentials have not been tested. Nevertheless, we expect these ion potential calculations to be quite accurate. For the molecular Rydberg states we use the exact same shape as their $1^2\Sigma_u^+$ asymptote, including a shallow well of about 70 cm^{-1} depth located at around 11 Å, and shift the curves down by the binding energy of the appropriate atomic Rydberg level.[38] In other words, because no other information is available, we make the assumption of a constant quantum defect along each Rydberg potential. Because the principal quantum numbers involved are fairly low ($n < 15$), we can characterize the Rydberg states in Hund's case (a) notation as $nl\ ^1\Lambda_u^{\pm}$ with the core electron in the antibonding $3s\sigma_u$ orbital. Before the last transition, the Na_2 molecule is in the $2^1\Pi_g$ state, which dissociates adiabatically into a Na(3s)−Na(3d) pair. Therefore, in a single electron picture, excitation can lead to both *n*p and *n*f atomic Rydberg states with the latter expected to have by far the larger oscillator strength. For the model calculations shown in Figure 3, we used only *n*f-Rydberg states. Varying which asymptotic atomic

angular momentum states, and thus which Rydberg states are involved, does change the details of the energy dependence of the Na^+:Na_2^+ ratios. However, this variation is, with some minor exceptions, no larger than the variation shown in Figure 3 due to changing the autoionization time scale. It has no significant effect on the overall orders of magnitude of the Na^+:Na_2^+ ratios. This is not surprising, because the distance independence of the quantum defect implies that, at least in the current constraints of our model, changing the Rydberg angular momentum is the same as changing the binding energy. And because there are always some Rydberg states within at least a few hundred cm^{-1} energy range, the overall outcome is not grossly impacted.

Once we have chosen a set of Rydberg potential curves, we calculate relative Franck−Condon densities for excitation from each of the initial $2^1\Pi_g$ vibrational levels and the appropriate photon energy hf_2. After being weighted by a scaling factor $1/n^3$ to account for the expected variation of transition strength with effective principal quantum number n, these calculated density numbers are then used as the relative w_n by which subsequently calculated ion yields along each single Rydberg curve are multiplied. To compare ion yields involving different initial vibrational levels in the $2^1\Pi_g$ and $A^1\Sigma_u^+$ states, we also include Franck−Condon factors and transition dipole moments[39] for the corresponding transitions. Typically, about six Rydberg states contribute significantly to the total ion yield. These yields are obtained following the idea outlined at the beginning of this section. First, we assume a constant autoionization lifetime τ_n for each Rydberg state. In quantum mechanical terms, we assume that the width of the autoionizing region, the region inside of point C in Figure 4, is constant. Obviously, the autoionization time can always be expressed in units of the Bohr orbit period associated with the corresponding atomic Rydberg state, i.e., $\tau_n = c_n n^3 \tau_B$, where $\tau_B = 0.152$ fs is the Bohr period of the ground state of hydrogen. In our model, we make the further assumption that all molecular Rydberg states have the same global scaling constant so that $c_n = c$ for all values of n considered and $\tau_n = n^3\tau_{AI}$ with $\tau_{AI} = c\tau_B$. Excitation to point A in Figure 5 occurs at time $t = 0$. At any given subsequent time t, the surviving fraction of dissociating neutral Rydberg molecules is then given by the value of $\exp(-t/\tau_n)$. If we designate by t_{AC} the time for arriving at the point where all autoionization stops (point C in Figure 5) and by t_{AB} the time for arriving at the critical distance that separates atomic and molecular ion formation (somewhere between points A and C and near B in Figure 5), then the atomic and molecular ion yields, $I_1(\Delta E)$ and $I_2(\Delta E)$ respectively, and from them the Na^+:Na_2^+ ratios can be calculated from expression

$$I_1(\Delta E) = \sum_n w_n \left(e^{-t_{AB}/\tau_n} - e^{-t_{AC}/\tau_n}\right) \quad (1.2)$$

and

$$I_2(\Delta E) = \sum_n w_n \left(1 - e^{-t_{AB}/\tau_n}\right) \quad (1.3)$$

Note that the previously defined weight factor w_n depends on the particular transition and that the dissociation times t_{AB} and t_{AC} vary with both n and excess energy ΔE involved. If atomic and molecular ion yield predictions of eqs 1.2 and 1.3 were to be compared to experimental findings, we would have to introduce an additional overall scaling factor. However, model predictions for the Na^+:Na_2^+ ratio, $I_1(\Delta E)/I_2(\Delta E)$, do not require such a factor as long as we correct (as we do) experimental ratios for detection efficiency variations. By minimizing χ^2 for all the differences between observed and calculated ratios

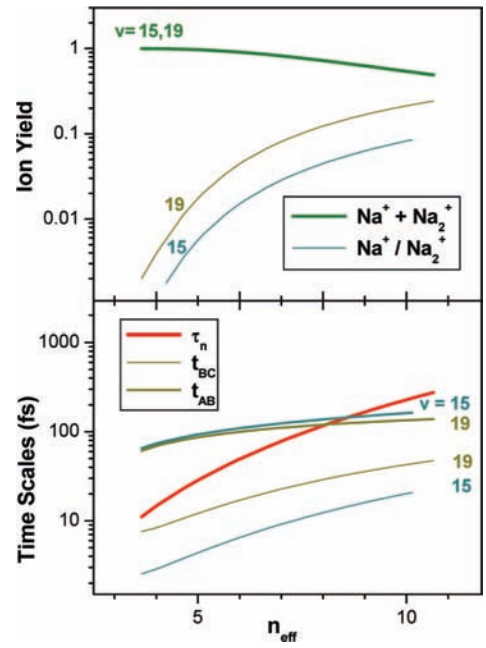

Figure 6. Sample results of model calculation: (upper panel) ion yield and ratio for excitation from $v' = 16$ in the $A^1\Sigma_u^+$ state to $v = 15$ and 19 in the $2^1\Pi_g$ state; (lower panel) variation of characteristic time scales with effective principal quantum number of corresponding repulsive Rydberg states. Optimized autoionization lifetime τ_n, dissociation times t_{AB} and t_{BC} that are spent between points A and B, and B′ and C, respectively (see Figure 5).

simultaneously, the single remaining adjustable factor, the global scaling constant for the autoionization lifetime, is found to be $c = 1.5$. Figure 3 shows Na^+:Na_2^+ ratios calculated with this scaling factor for each transition of the excitation sequences starting in $v' = 16-18$. Also shown are two other results for scaling factors that are respectively 20% higher and lower. Even such a relatively small change of the autoionization rate changes the ion ratio significantly. The next section will discuss some of the underlying reasons for this sensitivity as well as the overall performance of our model.

Discussion

Figure 6 summarizes the results of the model for excitation of the $v' = 16$ vibrational level of the $A^1\Sigma_u^+$ state to $v = 15$ and 19 levels of the $2^1\Pi_g$ state. In this case, rotationally averaged excess energies ΔE are 331 ± 27 and 1048 ± 25 cm^{-1}, respectively. The bottom panel shows the important timescales for these excess energies: the optimized autoionization time $\tau_n = n^3\tau_{AI}$ with $\tau_{AI} = 0.23 \pm 0.05$ fs, which is of course independent of ΔE; the time t_{AB} during which molecular ion formation is possible, i.e., the time when the critical distance is reached where the kinetic energy accumulated on the repulsive Rydberg curve is equal to the local binding energy of the $X^2\Sigma_g^+$ ground state; the time span $t_{BC} = t_{AC} - t_{AB}$ available for atomic ion production where t_{AC} is the time when the crossing point between neutral Rydberg and ground-state ion potentials is reached and autoionization is no longer possible. Figure 6 shows how these times vary as a function of the principal quantum number of the Rydberg state. Both dissociation times t_{AB} and t_{AC} increase with increasing quantum number when ΔE is kept constant because then the initial acceleration at point A is lower for Rydberg potentials with higher n (which is equivalent to climbing down the potential curve; see Figure 5). However, the effect is relatively small for t_{AB}, and, because the autoionization

time increases much more rapidly with n, the overall ion yield decreases with increasing n. This is clearly visible in the top solid line in the top panel of Figure 6, which shows the total ion yield ($Na^+ + Na_2^+$). On the scale used in the figure the total ion yields for $v = 15$ and 19 are indistinguishable as they differ by at most 2% in the range calculated. For each quantum number n, the ion yield and thus the ratio is easily calculated from the times in the bottom panel by eqs 1.2 and 1.3. The initial slowing of the dissociative motion of the Rydberg molecule with increasing quantum number n is further amplified for the atomic ion channel because the crossing point C moves out rather quickly on the shallower limb of the $X^2\Sigma_g^+$ potential (see Figure 5). As a result, the time t_{BC} during which atomic ion production is possible increases more rapidly with n than t_{AB} so that the Na^+:Na_2^+ ratios (two thin lines in upper panel of Figure 6) increase with principal quantum number even while overall ion yields decrease. This trend in the ion ratio is definitely borne out in our measurements. And for the optimized autoionization rate, also the agreement in overall magnitude of the ratio is satisfactory. Given the constraints and simplifications of our model it is not surprising that we do not capture details of the variation of the ratio with excess energy. However, it appears that our model also systematically underestimates the relative atomic ion yield in the mid energy range between 600 and 900 cm^{-1}. A trend of the Na^+:Na_2^+ ratio that runs flatter above about 500 cm^{-1} and steeper at energies below that value would appear to be in better agreement with the data. On the other hand, there are only three data points in this energy range and one needs to proceed with caution. We intend to explore this interesting process in more detail, including polarization dependences and fragment kinetic energy distributions. In the meantime, we have probably exhausted what can be gleaned from our data.

Conclusions

Excitation of vibrational levels $v = 16-18$ of the $2^1\Pi_g$ state with photons in the 620−655 nm wavelength range leads to formation of atomic Na^+ ions amounting to a few percent of total ion yield. We have measured the variation of the Na^+:Na_2^+ ion yield ratio as a function of excess energy above threshold for dissociative ionization. To a first approximation, the ratio rises from near zero at threshold to about 0.08 at the largest investigated energy of about 1500 cm^{-1} above threshold. No measurable differences could be discerned between the two rotational levels $J = 24$ and 30 observed in our experiments. Atomic ions are produced despite the fact that Franck−Condon densities for direct excitation into the continua associated with the $X^2\Sigma_g^+$ and $1^2\Sigma_u^+$ states are negligible. On the other hand, Rydberg states converging toward the repulsive $1^2\Sigma_u^+$ state provide large Franck−Condon overlap. Therefore, we developed and tested a semiclassical model that invokes competition between electronic autoionization and molecular dissociation to predict the variation of the atomic-to-molecular ion ratio as a function of excess energy. Adjusting the only free parameter of the model, a global scaling factor for the autoionization lifetime τ_n, comparison of model predictions to the experimental findings leads to a least-squares agreement for a value of $\tau_n = n^3\tau_{AI}$ with $\tau_{AI} = 0.23 \pm 0.05$ fs and n the effective principal quantum number of the Rydberg state involved. This corresponds to the Rydberg electron completing 1−2 orbits before being ejected into the continuum by autoionization. Our experiment is sensitive to principal quantum numbers from about $n = 5-10$; absolute autoionization lifetimes in this range are roughly 30−230 fs, respectively. These values are significantly shorter than the values of a few nanosecond reported[40] for Na_2 Rydberg states undergoing vibrational autoionization into the Na_2^+ $X^2\Sigma_g^+$ ($v = 1$) state. However, in our case, autoionization does not require electron−nucleus interaction and can be expected to proceed much faster. In a recent review[41] on NO predissociation, autoionization lifetimes are quoted in the same n^3-scaling form that we have applied here. Internal conversion and autoionization of Rydberg states in larger molecules are listed with τ_{AI} values between about 4.2 and 5.2 fs. And for Ar nd' autoionization, which requires an interaction between Rydberg and core electron similar to the one we invoke in our model, the reported τ_{AI} value is as small as 1.1 fs.

We have also recorded polarization dependent time-of-flight spectra that reveal kinetic energy and angular distributions of the Na^+ fragments. Although more detailed analysis is still needed, the variation of the TOF spectra with polarization change is consistent with an angular distribution that favors dissociation with the molecular axis aligned parallel to the laser polarization direction, i.e., consistent with parallel transitions. Furthermore, the observed widths of the TOF peaks are consistent with the maximum fragment energies predicted in our model. In summary, our experiments demonstrate that at least in this particular circumstance, nanosecond lasers can be used to gain insight into molecular and electron dynamics occurring at the femtosecond time scale.

References and Notes

(1) Morisset, S.; Pichl, L.; Orel, A. E.; et al. *Phys. Rev. A* **2007**, *76*, 042702.
(2) Carata, L.; Schneider, I. F.; Suzor-Weiner, A. *Philos. Trans. R. Soc., London, Ser. A* **1997**, *355*, 1677–1691.
(3) Florescu-Mitchell, A. I.; Mitchell, J. B. A. *Phys. Rep.-Rev. Sect. Phys. Lett.* **2006**, *430*, 277–374.
(4) Thiel, L.; Hotop, H.; Meyer, W. *J. Chem. Phys.* **2005**, *122*, 184309.
(5) Amelink, A.; Jones, K. M.; Lett, P. D.; et al. *Phys. Rev. A* **2000**, *61*, 042707.
(6) Bozek, J. D.; Furst, J. E.; Gay, T. J.; et al. *J. Phys. B* **2006**, *39*, 4871–4882.
(7) Glass-Maujean, M.; Klumpp, S.; Werner, L.; et al. *J. Phys. B* **2004**, *37*, 2677–2684.
(8) Hiyama, M.; Kosugi, N.; Nakamura, H. *J. Chem. Phys.* **1997**, *107*, 9370–9381.
(9) Kouchi, N.; Ukai, M.; Hatano, Y. *J. Phys. B* **1997**, *30*, 2319–2344.
(10) Laue, T. ; Pellegrini, P. ; Dulieu, O.; et al. *Eur. Phys. J. D* **2003**, *26*, 173−185.
(11) Magnier, S.; Millié, P. *Phys. Rev. A* **1996**, *54*, 204–218.
(12) Tennyson, J. *At. Data Nucl. Data Tables* **1996**, *64*, 253–277.
(13) Huynh, B.; Dulieu, O.; Masnou-Seeuws, F. *Phys. Rev. A* **1998**, *57*, 958–975.
(14) Baumert, T.; Gerber, G. *Isr. J. Chem.* **1994**, *34*, 103–114.
(15) Engel, V.; Baumert, T.; Meier, C. *Z. Phys. D* **1993**, *28*, 37. (1993).
(16) Baumert, T.; Engel, V.; Röttgermann, C.; et al. *Chem. Phys. Lett.* **1992**, *191*, 639–644.
(17) Haugstätter, R.; Goerke, A.; Hertel, I. V. *Z. Phys. D* **1990**, *16*, 61–70.
(18) Haugstätter, R.; Goerke, A.; Hertel, I. V. *Phys. Rev. A* **1989**, *39*, 5085–5091.
(19) Bakker, B. L. G.; Parker, D. H.; van-der-Zande, W. J. *Phys. Rev. Lett.* **2001**, *86*, 3272–3275.
(20) Black, K.; Delahunty, B.; Hüwel, L. *Phys. Rev. A* **1999**, *60*, 1179–1186.
(21) Delahunty, B. J.; Hüwel, L. *Phys. Rev. Lett.* **1998**, *80*, 1186–1189.
(22) Bergmann, K.; Hefter, U.; Hering, P. *Chem. Phys.* **1978**, *32*, 329–348.
(23) Wiley, W.; McLaren, I. *Rev. Sci. Instrum.* **1955**, *26*, 1150–1157.
(24) Whang, T.-J.; Wang, H.; Lyyra, A. M.; et al. *J. Mol. Spectrosc.* **1991**, *145*, 112–122.
(25) Camacho, J. J.; Pardo, A.; Poyato, J. M. L. *J. Phys. B* **2005**, *38*, 1935–1954.
(26) Qi, P.; Bai, J.; Ahmed, E.; et al. *J. Chem. Phys.* **2007**, *127*, 044301−044317.
(27) Baumfalk, R.; Buck, U.; Frischkorn, C.; et al. *J. Chem. Phys.* **1999**, *111*, 2595–2605.
(28) Zare, R. *Mol. Photochem.* **1972**, *4*, 1–37.

(29) Jones, K. M.; Maleki, S.; Bize, S.; et al. *Phys. Rev. A* **1996**, *54*, R1006−1009.

(30) Sansonetti, J. E.; Martin, W. C. *J. Phys. Chem. Ref. Data* **2005**, *34*, 1559–2259.

(31) O'Malley, T. T. *Phys. Rev.* **1966**, *150*, 150.

(32) Babenko, E.; Tapalian, C.; Smith, W. W. *Chem. Phys. Lett.* **1995**, *244*, 121–126.

(33) Magnier, S. Ph.D. Thesis, Physics Department, Université de Paris-Sud, Centre d'Orsay, Orsay, 1993, p 250.

(34) Magnier, S.; Masnou-Seeuws, F. *Mol. Phys.* **1996**, *89*, 711–735.

(35) Johann, C.; Kleinekathofer, U.; Tang, K. T.; et al. *Chem. Phys. Lett.* **1996**, *257*, 651–657.

(36) Johann, C.; Patil, S. H.; Tang, K. T.; et al. *Chem. Phys. Lett.* **1998**, *295*, 158–166.

(37) Blange, J. J.; Urbain, X.; Rudolph, H.; et al. *J. Phys. B* **1997**, *30*, 565–581.

(38) Ralchenko, Y. ; Kramida, A. E.; Reader, J. ;NIST ASD Team. NIST Atomic Spectra Database, version 3.1.4; National Institute of Standards and Technology: Gaithersburg, MD, 2008; http://physics.nist.gov/asd3.

(39) Magnier, S. Private communication.

(40) Bordas, C. ; Brevet, P. F.; Broyer, M. ; et al. *Phys. Rev. Lett.* **1988**, *60*, 917−920.

(41) Bixon, M.; Jortner, J. *J. Chem. Phys.* **1996**, *105*, 1363–1382.

JP802342D